ChemSusChem

Research Article
doi.org/10.1002/cssc.202102390

Chemistry Europe
European Chemical Societies Publishing

www.chemsuschem.org

In-Situ Growth of Mn_3O_4 Nanoparticles on Nitrogen-Doped Carbon Dots-Derived Carbon Skeleton as Cathode Materials for Aqueous Zinc Ion Batteries

Tian-Bing Song,[a] Zun-Hui Huang,[a] Xiao-Qing Niu,[a] Xi-Rong Zhang,[a] Ji-Shi Wei,[a] and Huan-Ming Xiong*[a]

Mn_3O_4 is a promising cathode material for aqueous zinc ion batteries (ZIBs) which is a new type of low cost, eco-friendly, high security energy storage system, while those previously reported electrochemical capacities of Mn_3O_4 are far from its theoretical value. In this work, Mn_3O_4 nanoparticles and nitrogen-doped carbon dots (NCDs) are synthesized together through an in-situ hydrothermal route, and then calcined to be a nanocomposite in which Mn_3O_4 nanoparticles are anchored on a nitrogen-doped carbon skeleton (designated as Mn_3O_4/NCDs). Although the carbon content is only 3.9 wt.% in the Mn_3O_4/NCDs, the NCDs-derived carbon skeleton provides an electrically conductive network and a stable structure. Such a special nanocomposite has a large specific surface area, plenty of active sites, excellent hydrophilicity and good electronic conductivity. Owing to these structural merits, the Mn_3O_4/NCDs electrode exhibits a preeminent specific capacity of 443.6 mAh g^{-1} and 123.3 mAh g^{-1} at current densities of 0.1 and 1.5 A g^{-1} in ZIBs, respectively, which are far beyond the bare Mn_3O_4 nanoparticles synthesized under the similar condition. The electrochemical measurement results prove that carbon dots, as a new type of carbon nanomaterials, have strong ability to modify and improve the performance of existing electrode materials, which may push these electrode materials forward to practical applications.

Introduction

Aqueous rechargeable batteries based on Zn^{2+}, Mg^{2+}, Al^{3+} or Fe^{3+} ions have become a research hotspot recently because of their low manufacturing cost, reliable safety, and environmentally benign nature. Among these new batteries, zinc ion batteries (ZIBs) are constructed by zinc metal anodes, aqueous electrolytes and various cathode materials.[1] Zinc metal anodes have the merits of abundant resources, high theoretical capacity of 820 mAh g^{-1}, suitable redox potential and facile handling process, while aqueous electrolytes have higher conductivity, fewer hazards and greater safety compared with the organic electrolytes.[2] Since choices are limited for both anodes and electrolyte, research in ZIBs at present focuses on cathode materials, such as manganese-based oxides, Prussian blue, vanadium-based materials and molybdenum-based materials.[3] Among them, manganese oxides have attracted extremely high attention because of their abundant storage on earth, green chemistry and high discharge voltage.[4] Many Zn/MnO_2 batteries have been reported with good electrochemical performance in the past years.[5] As a promising candidate, Mn_3O_4 with the chemical formula of $Mn^{II}Mn^{III}{}_2O_4$, have shown both considerable capacity and high voltage. However, these manganese oxides always suffer from poor conductivity and large volume expansion during cycling, which result in electrode pulverization, collapse of the structure and rapid capacity fading in practical ZIBs.[6]

Various strategies have been devised to overcome the intrinsic drawbacks of Mn_3O_4 materials, such as nanostructure design, valence engineering and carbon coating. For instance, Kang and coworkers reported that the electrochemically synthesized Mn_3O_4 nanoparticles showed a high specific capacity as the cathode material for ZIBs.[7] However, the nanostructure design inevitably reduces the tap density, resulting in a low energy density of ZIBs. Wang et al. realized valence engineering by controlling oxygen defects in Mn_3O_4@C nanorod arrays, which exhibited an ultra-long cycle life and a high capacity of 396.2 mAh g^{-1} at 0.2 A g^{-1}.[8] However, the valence engineering generally demands a complicated experimental procedure, multiple steps and strict control of the reaction conditions, which leads to a marked increase in costs. Chen and coworkers suggested a simple and efficient method to synthesize porous cube-like Mn_3O_4@C composite material with good electrochemical performance.[9] In general, after coating carbon layers, the composite materials will have large specific surface areas, excellent conductivity and long-term stability. Besides, the bulk carbon materials like graphene, carbon nanotubes and porous carbon, can be mixed with Mn_3O_4 to form nanocomposites. Unfortunately, the synthesis of graphene and activation of carbon nanotubes often require complex, hazardous and time-consuming process. As for the porous carbon, the connections between Mn_3O_4 and porous

[a] T.-B. Song, Z.-H. Huang, X.-Q. Niu, X.-R. Zhang, Dr. J.-S. Wei, Prof. Dr. H.-M. Xiong
Department of Chemistry and Shanghai Key Laboratory of Molecular Catalysis and Innovative Materials
Fudan University
Shanghai 200438, P. R. China
E-mail: hmxiong@fudan.edu.cn

Supporting information for this article is available on the WWW under https://doi.org/10.1002/cssc.202102390

carbon are inhomogeneous and loose, so the protection for Mn_3O_4 from carbon is incomplete and unstable.

Carbon dots (CDs), with particle size of several nanometers and high dispersibility in various solvents, have received extensive research interest recently in many energy storage devices owing to their impressive physical and chemical properties.[10] In general, CDs have graphited cores and amorphous surfaces with functional groups, various defects and doped elements. Such structural merits endow CDs with special ability to combine with inorganic solids tightly, protect the host completely, improve the conductivity and even control the growth and morphology of the composites.[10d,11] For example, our group prepared flower-like CDs/$NiCo_2O_4$ nanocomposites with excellent performance in supercapacitors previously.[12] Using CDs as both coating and incorporating materials, the shortcomings of the above mentioned methods could be overcome once and for all.

Herein, we used nitrogen-doped CDs (NCDs) synthesized by a solvothermal method to construct carbon skeletons, where Mn_3O_4 nanoparticles grew *in situ* at high temperature to form the final Mn_3O_4/NCDs nanocomposite. Such a composite has abundant functional groups (–COOH, –NH, –OH, etc.) on the surface which benefit its contact with the aqueous electrolyte. The tight protection of Mn_3O_4 nanocrystals by carbon enhances both the conductivity and stability, leading to excellent electrochemical performance as a cathode in aqueous ZIBs. Our Mn_3O_4/NCDs composite exhibits an ultrahigh capacity of 443.6 mAh g^{-1} at 100 mA g^{-1}, and a capacity of 123.3 mAh g^{-1} at a high current density of 1500 mA g^{-1}, indicating a remarkable rate capability.

Scheme 1. Schematic illustration for the preparation of carbon skeleton, Mn_3O_4 and Mn_3O_4/NCDs.

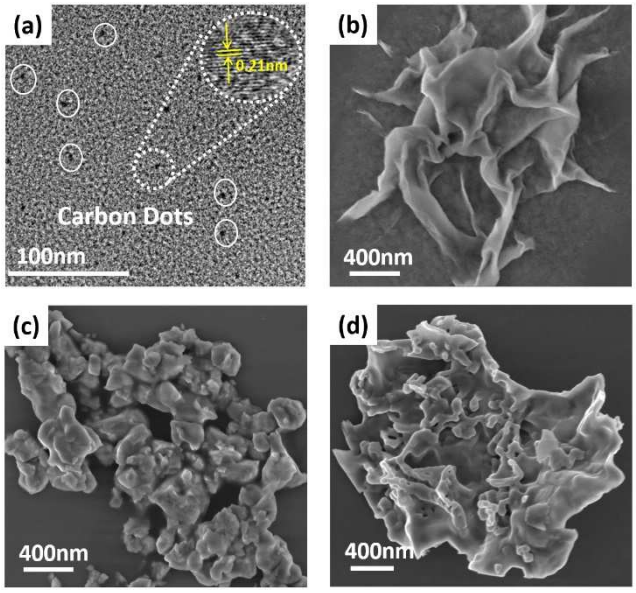

Figure 1. (a) TEM and HRTEM images of NCDs; SEM images of (b) NCDs-derived carbon skeleton, (c) Mn_3O_4 and (d) Mn_3O_4/NCDs.

Results and Discussion

The preparation processes of the nitrogen-doped carbon skeletons, Mn_3O_4 and Mn_3O_4/NCDs are illustrated in Scheme 1. NCDs were synthesized from solution A which contains citric acid and ethylenediamine by a typical hydrothermal reaction. Afterward, NCDs were calcined to carbon skeleton at 700 °C. The Mn-benzenetricarboxylic (Mn-BTC) was synthesized by the coordination reaction between manganese nitrate and 1, 3, 5-benzenetricarboxylic acid (solution B + C), and then calcined to generate irregular Mn_3O_4 particles. When the solution A + B + C was treated by the same hydrothermal process and the subsequent calcination, the product was Mn_3O_4 nanoparticles deposited on carbon skeleton, which was designated as Mn_3O_4/NCDs composite. Clearly, the *in situ* grown NCDs have inhibited the growth of Mn_3O_4 and anchored Mn_3O_4 nanoparticles on the final carbon skeleton.

The transmission electron microscopy (TEM) image (Figure 1a) shows that NCDs are monodispersed with particle sizes of about 5 nm. The high-resolution TEM (HRTEM) image (inset of Figure 1a) displays the distinct lattice fringes of 0.21 nm that can be assigned to the (100) planes of graphite. Besides, the X-ray diffraction (XRD) pattern of NCDs (Figure S1) shows a strong peak at around 25°, corresponding to the typical (002) plane of the graphite structure.[13] The surface states of NCDs were studied by Fourier transform infrared (FT-IR) spectroscopy and X-ray photoelectron spectroscopy (XPS), respectively. FT-IR spectrum (Figure S2a) confirms the presence of various functional groups on NCDs. The bands at 3430, 1710, 1648 and 1385 cm^{-1} are ascribed to O–H/N–H (hydroxyl/amino), C=O (carbonyl), C=N (aromatic nucleus) and C–N vibrations, respectively.[14] Correspondingly, XPS spectra in Figure S2b show C 1s, N 1s and O 1s peaks at 284.6, 398.2 and 531.6 eV, respectively, indicating that nitrogen has been doped into CDs successfully. The high-resolution spectrum of C 1s (Figure S2c) shows the presence of COOH, C=O, C=C/C–C and C–O/C–N functional groups. The N 1s spectrum (Figure S2d) was deconvo-

luted into three peaks, representing graphitic N, pyrrolic N and pyridinic N, respectively.[15] These results are in agreement with the above FT-IR analyses.

Scanning electron microscopy (SEM) analysis was carried out to investigate the morphology of the calcined NCDs, the as-synthesized Mn_3O_4 and the calcined Mn_3O_4/NCDs. In Figure 1b, it can be clearly observed that NCDs self-assembled into three dimensional skeleton structures with rough surface at high temperature. Figure 1c shows the as-synthesized Mn_3O_4 have large particle sizes because of agglomeration, and these aggregates are discontinuous. In contrast, the particle sizes of the Mn_3O_4/NCDs are smaller and the composites are smooth and continuous. According to the above XPS and FT-IR analyses, the surface of NCDs have residual hydrophilic groups and a great quantity of active sites which can more effectively adsorb metal ion precursors during reactions, resulting in the Mn_3O_4 nanocrystals anchored on the carbon skeleton. To verify this point, we further compared the photos of Mn-BTC and Mn-BTC/NCDs under daylight and ultraviolet (UV) light, respectively. The photo in Figure S4 verifies the existence of fluorescent NCDs. The transparent solution of Mn-BTC/NCDs proves that NCDs are able to adhere and protect Mn species, which contributed to the formation of a homogeneous Mn_3O_4/NCDs composite finally.

The intricate morphologies of both Mn_3O_4 and Mn_3O_4/NCDs observed via TEM and HRTEM are shown in Figure 2. The as-prepared Mn_3O_4 particles are irregular and agglomerated, with lattice spacing of 0.492 nm and 0.164 nm, corresponding to the (101) and (303) planes of Mn_3O_4, respectively. Energy dispersive spectroscopy (EDS) mapping was carried out to examine the existence and distribution of each element. The results in Figure S3 prove that Mn and O elements are distributed homogeneously in the Mn_3O_4 nanoparticles, while a trance amount of C element may be from the carbon membrane on the copper grid. In contrast, TEM (Figure 2c) and HRTEM (Figure 2d) images of Mn_3O_4/NCDs reveal that the Mn_3O_4 nanocrystals grown on the carbon skeleton are significantly smaller than those in Figure 2a. In addition, the inset of Figure 2d shows the selected area electron diffraction (SAED) pattern of Mn_3O_4/NCDs, which confirms the tetragonal structure of Mn_3O_4 (JCPDS Card no. 24–0734). Furthermore, the EDS mapping of Mn_3O_4/NCDs in Figure 2e shows all elements (Mn, O, C and N) are homogeneously distributed in the sample, which means nitrogen have been doped into the carbon skeleton successfully and Mn_3O_4 nanocrystals have located on the carbon skeleton homogeneously. These structural features will benefit the electrochemical measurements.

The XRD patterns of the Mn_3O_4 and Mn_3O_4/NCDs samples are compared with the reference of Mn_3O_4 with tetragonal space group I41/amd in Figure 3a. Both samples are in good agreement with the reference, indicating that NCDs do not introduce impurity phase to Mn_3O_4. In Figure 3b, the crystal of Mn_3O_4 has a tetragonal spinel structure, in which Mn^{II} and Mn^{III} ions separately occupy the tetragonal (4a) sites and the octahedral (8d) sites in the intervening distorted cubic close-packed arrays of oxygen atoms.[16] Figure 3c shows Raman spectra of the carbon skeleton, Mn_3O_4 and Mn_3O_4/NCDs. The Mn_3O_4 and Mn_3O_4/NCDs have peaks at 250–700 cm^{-1}, which could be indexed to the Mn–O vibrations, while two broad bands at 1351 and 1597 cm^{-1} are observed in the carbon skeleton and the Mn_3O_4/NCDs sample, corresponding to the disordered band (D) and graphitic band (G) of carbon materials, respectively.[17] To quantify the contents of Mn_3O_4 and NCDs in the composite, thermogravimetric (TGA) measurement was carried out in air from 50 to 950 °C at a rate of 5 °C min^{-1}

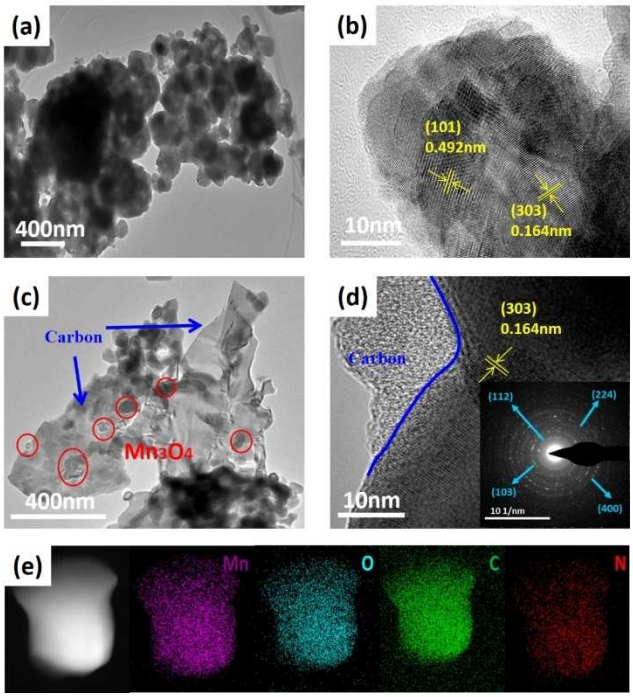

Figure 2. (a) TEM and (b) HRTEM images of Mn_3O_4; (c) TEM and (d) HRTEM images of Mn_3O_4/NCDs (inset is SAED pattern); (e) Elemental mapping images of Mn_3O_4/NCDs.

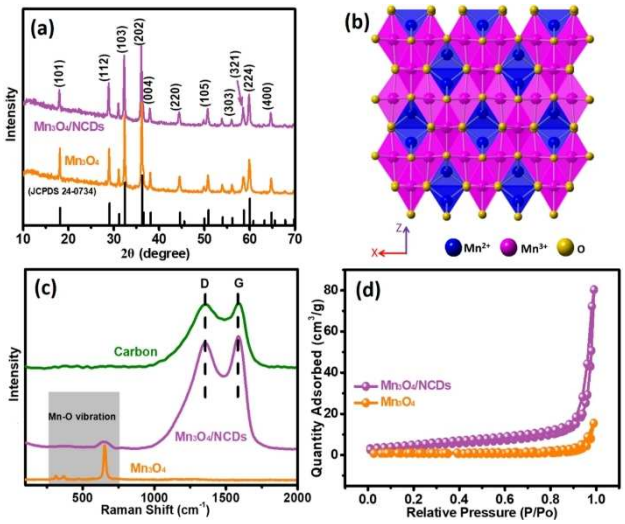

Figure 3. (a) XRD patterns of Mn_3O_4/NCDs and Mn_3O_4; (b) The schematic illustration of Mn_3O_4 crystal structure; (c) Raman and (d) N_2 adsorption-desorption isotherms of Mn_3O_4/NCDs and Mn_3O_4.

(Figure S5). It is surprising that the weight loss of the Mn_3O_4/NCDs sample is only about 3.9%, which means such a tiny amount of carbon could modify Mn_3O_4 significantly. More importantly, the high content of Mn_3O_4 in the composite will render a high specific capacity as an electrode material. Since the specific surface area is also an important parameter for an electrode material, the N_2 adsorption-desorption isotherm data of Mn_3O_4 and Mn_3O_4/NCDs samples were collected. As shown in Figure 3d, the specific surface area of Mn_3O_4 and Mn_3O_4/NCDs were measured to be 16.0 $m^2 g^{-1}$ and 45.5 $m^2 g^{-1}$ by Brunauer-Emmett-Teller (BET) method. Therefore, incorporation of carbon material endows the composites with a much larger surface area than the original Mn_3O_4, which not only provides more contact area between the active material and electrolyte, but also facilitates the transport of zinc ions.

XPS characterization was employed to gather information of the chemical compositions and the oxidation states in the Mn_3O_4 and Mn_3O_4/NCDs samples. As shown in Figure 4a and Table S1, the full survey of Mn_3O_4 obviously shows peaks for Mn, O and C elements, while the full spectrum of Mn_3O_4/NCDs has additional signals of N element (content is 1.64%, also see the inset), in accord with the EDS mapping results (Figure 2e). The Mn 2p spectrum in Figure 4b indicates that Mn has a mixed-valence state, including Mn^{II} (640.7 and 652.5 eV), Mn^{III} (642.5 and 654.1 eV) and Mn^{IV} (645 and 656.4 eV). The Mn^{IV} may result from the surface oxidation.[18] The high-resolution O 1s spectrum (Figure 4c) has two peaks at 529.8 and 531.6 eV, representing the Mn–O–Mn bond and the O–H bond of adsorbed water.[19] The high-resolution C 1s spectrum can be resolved into four types (Figure 4d), representing C–C (284.8 eV), C–O/C–N (285.8 eV), C=O (287.4 eV) and COOH (288.8 eV).[15b] These results are in agreement with the FT-IR analyses of NCDs, indicating that carbon skeletons are derived from NCDs.

The electrochemical properties of both Mn_3O_4 and Mn_3O_4/NCDs samples are presented in Figure 5 and Figure S6. The

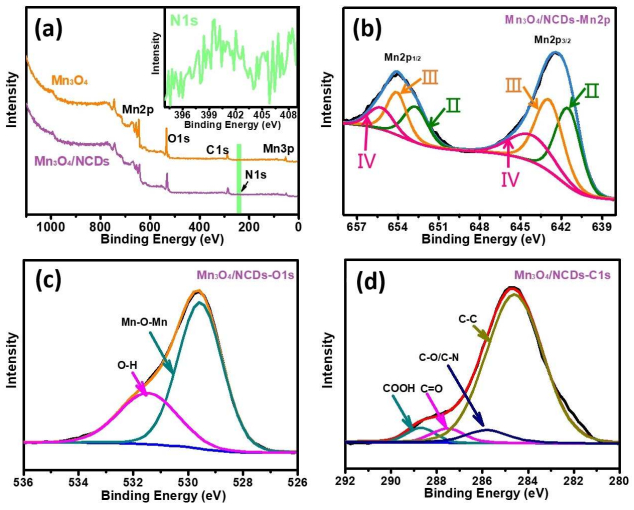

Figure 4. (a) XPS of Mn_3O_4 and Mn_3O_4/NCDs; High resolution XPS analyses for (b) Mn 2p, (c) O 1s, (d) C 1s of Mn_3O_4/NCDs.

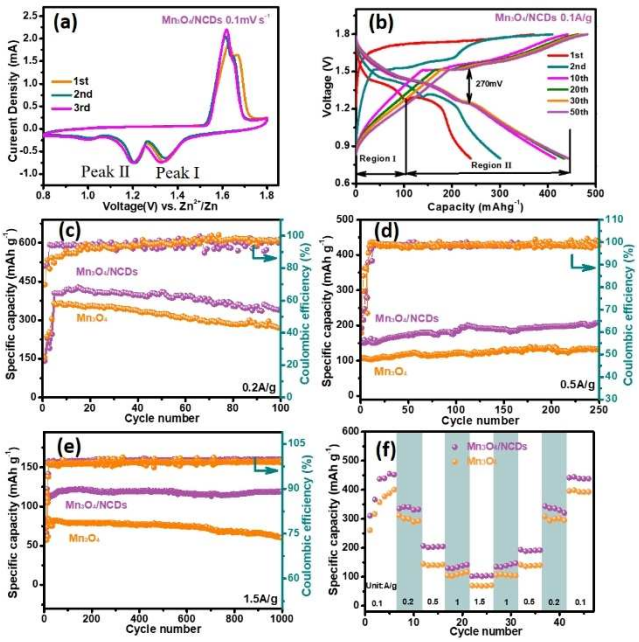

Figure 5. Electrochemical measurements of Mn_3O_4 and Mn_3O_4/NCDs. (a) CV curves of Mn_3O_4/NCDs at a scan rate of 0.1 mV s^{-1}; (b) Charge-discharge curves of Mn_3O_4/NCDs at 0.1 A g^{-1}. Comparison of the cycling performance of Mn_3O_4 and Mn_3O_4/NCDs at (c) 0.1 A g^{-1}, (d) 0.5 A g^{-1} and (e) 1.5 A g^{-1}; (f) Rate properties of Mn_3O_4 and Mn_3O_4/NCDs.

cyclic voltammetry (CV) curves of Mn_3O_4/NCDs electrode were recorded at a scan rate of 0.1 mV s^{-1}, as shown in Figure 5a. Two initial reduction peaks emerged at 1.33 (peak I) and 1.21 V (peak II), respectively. The intensity of the reduction peaks gradually increased during scans because of the phase transition, and the oxidation peaks overlapped with each other at around 1.62 V. Particularly, the consistency of the initial CV curves were reasonably well, suggesting a reversible and low polarization process of Mn_3O_4/NCDs cathode. Figure 5b and Figure S6 show the galvanostatic charge/discharge curves of Mn_3O_4/NCDs and Mn_3O_4 at 0.1 A g^{-1}, respectively. The manganese-based materials all have the electrochemical activation process and phase transition from Mn_3O_4 to MnO_2 in the initial several cycles, which leads to a gradual increase in capacity. The capacity of Mn_3O_4/NCDs is up to 443.6 mAh g^{-1} after 50 cycles, while the capacity of Mn_3O_4 is only 310.3 mAh g^{-1} during the same cycles. Furthermore, the typical discharge curve could be identified into two distinct regions. This observation is consistent with literature reports in that Region I and Region II are recognized as the H^+ and Zn^{2+} insertion process, respectively. Meanwhile, Region I and Region II correspond to Peak I and Peak II of the CV curves, respectively.[20] In comparison with the galvanostatic charge/discharge curves of Mn_3O_4 (Figure S6), the Mn_3O_4/NCDs data show much longer discharge platforms. Particularly in Region I, the Mn_3O_4/NCDs shows a much higher discharge capacity than that of Mn_3O_4, which reveals the higher electrochemical activity and the easier H^+ insertion for Mn_3O_4/NCDs. In addition, the voltage platform difference between the charging/discharging curves after 50 cycles of Mn_3O_4/NCDs and

Mn_3O_4 increase from 270 mV to 295 mV, indicating the smaller polarization of the Mn_3O_4/NCDs material.

The cycling properties of Mn_3O_4 and Mn_3O_4/NCDs electrodes were investigated at various current densities, and the Mn_3O_4/NCDs electrode presented higher specific capacities (Figure 5c–e). At a current density of 0.2 A g^{-1} (Figure 5c), Mn_3O_4/NCDs and Mn_3O_4 retained reversible specific capacities of 325.1 and 282.6 mAh g^{-1} after 100 cycles and corresponding capacity retentions of 86.6% and 80.7%, respectively. When a larger current density of 0.5 A g^{-1} was applied, the Mn_3O_4/NCDs sample exhibited even better properties than its counterpart (Figure 5d). In the meantime, the Mn_3O_4/NCDs sample showed excellent coulombic efficiency as the cycle numbers increased to 250. After 1000 cycles at a current density of 1.5 A g^{-1}, the capacity of Mn_3O_4/NCDs was still 123.3 mAh g^{-1}, while the capacity of Mn_3O_4 was only 82.7 mAh g^{-1} (Figure 5e). Meanwhile, the cycling stability and specific capacities of Mn_3O_4/NCDs was also much superior to the previous reported Mn_3O_4 cathodes (Table S2). In order to further explore the rate performance of both samples, measurements were carried out at current densities from 0.1 to 2 A g^{-1}, as shown in Figure 5f. The Mn_3O_4/NCDs delivered discharge capacities of 443.2, 370.2, 227.5, 146.3 and 98.8 mAh g^{-1}, respectively. When the current density turned back to 0.1 A g^{-1}, the capacity of Mn_3O_4/NCDs returned to 432.9 mAh g^{-1}, implying a remarkable reversibility. As control, Mn_3O_4 showed much smaller capacities of 377, 300.3, 164.2, 100.6 and 52.4 mAh g^{-1}, respectively. Although the carbon content in Mn_3O_4/NCDs is only about 3.9 wt.%, the Mn_3O_4/NCDs electrode exhibited much better electrochemical properties than Mn_3O_4, because the NCDs derived carbon skeleton not only increased the electron conductivity so as to realize a good rate performance, but also accelerated Zn^{2+} migration through the porous structure with enlarged surface areas.

To further explore the effect of NCDs on zinc storage, electrochemical impedance spectroscopy (EIS) was measured for Mn_3O_4 and Mn_3O_4/NCDs at frequencies from 100 to 0.01 Hz. The semicircle in the Nyquist plots indicated the charge-transfer resistance (*R*ct) between the electrode and the electrolyte. As depicted in Figure 6a, the *R*ct of Mn_3O_4/NCDs electrode (404.7 Ω) was much smaller than that of the Mn_3O_4 electrode (710.2 Ω), which confirms that the NCDs-derived carbon skeleton can improve the contact between Mn_3O_4/NCDs electrode and electrolyte. Moreover, the *R*s of Mn_3O_4/NCDs (2.243 Ω) was also smaller than that of Mn_3O_4 (6.863 Ω) samples, indicating that the NCDs modification can improve the hydrophilicity of the electrode (Figure S8). Figure 6b shows the Nyquist plots of the Mn_3O_4/NCDs electrode after different charge-discharge cycles. After 5, 20, 35 and 50 cycles, the R_{ct} values of Mn_3O_4/NCDs was 404.7, 360, 318.8, 254.1 and 253.7 Ω, respectively, which are also shown in Table S3. It is interesting that the R_{ct} value of Mn_3O_4/NCDs decreases gradually when the cycle number increases, which means the contact between the electrode and electrolyte becomes better and better with the increase in cycle number. This process can be regarded as the electrode activation during cycles.

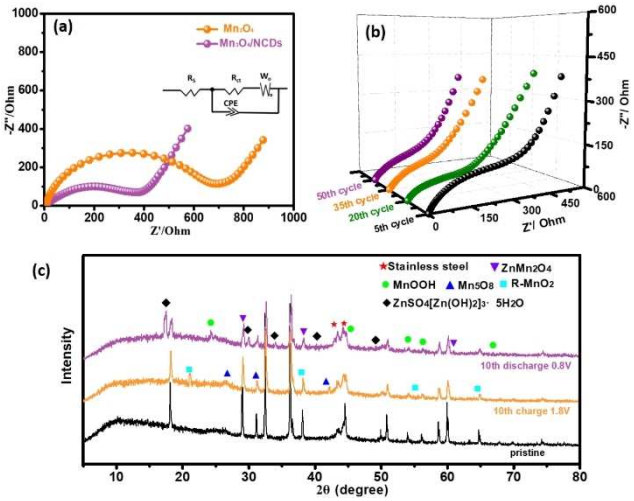

Figure 6. (a) EIS of Mn_3O_4 and Mn_3O_4/NCDs fresh electrodes; (b) EIS of Mn_3O_4/NCDs electrode after 5, 20, 35, 50 cycles at charge state; (c) *Ex situ* XRD of Mn_3O_4/NCDs at pristine/charge/discharge states during the 10th cycle.

The ex-situ XRD and galvanostatic intermittent titration technique (GITT) were carried out to understand the mechanism of zinc ions extraction/intercalation from/into the Mn_3O_4/NCDs materials after 10 charge/discharge cycles. Figure 6c shows the ex-situ XRD pattern of the electrode in different states. Compared with standard XRD patterns of Mn_3O_4, Mn_5O_8 and R-MnO_2 (ramsdellite MnO_2), diffraction peaks were observed during charging process from 0.8 to 1.8 V, which indicates phase transformation according to the following chemical reaction (1):

$$2Mn_3O_4 \rightarrow Mn_5O_8 + Mn^{2+} + 2e^- \quad (1)$$

Then Mn_5O_8 transformed to R-MnO_2 duo to dissolution of Mn^{2+} and insertion of H_2O on the basis of the following chemical reaction (2):

$$Mn_5O_8 + xH_2O \rightarrow 4MnO_2 \cdot xH_2O + Mn^{2+} + 2e^- \quad (2)$$

During the discharge process, the diffraction peaks at 16.5°, 31.8°, 34.7°, 40.7° and 48.7° could be assigned to $ZnSO_4[Zn(OH)_2]_3 \cdot 5H_2O$ at the full discharge. Meanwhile, the characteristic peaks of MnOOH phase appeared at 25.6°, 45.12°, 54.1°, 57.34° and 66.8°. The appearance of $ZnSO_4[Zn(OH)_2]_3 \cdot 5H_2O$ and MnOOH phase can be attributed to H^+ intercalation. Another set of diffraction peaks that appear at 29.3°, 39.3° and 60.0° belong to $ZnMn_2O_4$. The formation of $ZnMn_2O_4$ is attributed to intercalation of Zn^{2+}.[21] According to the discharge GITT profiles in Figure S9, the Mn_3O_4/NCDs materials exhibited high diffusion coefficients of 3.9×10^{-10} $cm^2 s^{-1}$ for D_{H+} (Region I) and 4.8×10^{-11} $cm^2 s^{-1}$ for D_{Zn2+} (Region II). In other words, Region I and Region II of the galvanostatic charge-discharge curve can be regarded as the H^+ and Zn^{2+} insertion process.

Conclusion

A new nanocomposite, Mn_3O_4 nanoparticles anchored on a carbon skeleton which is derived from nitrogen-doped carbon dots (NCDs), was synthesized through a facile hydrothermal route and a subsequent calcination. Such a Mn_3O_4/NCDs composite exhibited much better electrochemical performance than the bare Mn_3O_4 nanoparticles when they were used as electrode materials in zinc ion batteries (ZIBs), including high specific capacity, good reversibility and long cycle life. Mn_3O_4/NCDs showed a high specific capacity of 443.6 mAh g^{-1} after 50 cycles at 0.1 A g^{-1}, a good cycling stability with 86.6% capacity retention over 100 cycles at 0.2 A g^{-1}. Even at the current density of 1.5 A g^{-1}, it retained a capacity of 123.3 mAh g^{-1} after 1000 cycles. Such outstanding performance is ascribed to the structural merits of Mn_3O_4/NCDs composite, including large surface area, conductive network, good hydrophilicity and stable volume changes during cycles. Therefore, our present work has proved that carbon dots have strong ability to modify and improve the performance of Mn_3O_4 electrode materials, which may push these electrode materials forward to practical applications in ZIBs.

Experimental Section

Synthesis of Mn_3O_4/NCDs composite

Mn_3O_4/NCDs composite material was prepared via a convenient *in situ* solvothermal reaction followed by a thermal treatment. Before reactions, 700 μL of ethylenediamine and 2 g of citric acid were added in 3 mL of deionized water, which is designated as solution A. 10 mL of manganese nitrate solution (50 wt. % in H2O) were dissolved in 10 mL of methanol, which was named solution B. 0.131 g of 1, 3, 5-benzenetricarboxylic acid and 0.265 g of polyvinyl pyrrolidone were dissolved together in 10 mL of methanol, which was labelled as solution C. To prepare Mn_3O_4/NCDs, the solution A, B and C were mixed together and transferred into a Teflon-lined stainless-steel autoclave for 5 h heating at 160 °C. Afterwards, the resulting solution was added dropwise into ethanol to collect the precipitate by centrifugation. The precipitate is Mn-BTC/NCDs precursor, which was washed by ethanol and further dried in a vacuum oven. The dried powder was calcined in a tube furnace at 700 °C for 5 h in air to obtain the final Mn_3O_4/NCDs composite. To prepare Mn_3O_4 as control, only the solution B and C were treated by the above procedures. To prepare nitrogen-doped carbon skeletons solely, only the solution A was used for the treatment.

Characterization

The morphologies and structures of all materials were characterized by HRTEM (FEI Tecnai G2 F20 S-TWIN) and field emission SEM (FE-SEM, Zeiss Supra 55). The XRD patterns were recorded using a Bruker D2 Endeavor X-ray diffractometer to analyze the crystal phase composition of the samples in a range of 10°–70°. FT-IR spectra were collected on ThermoFisher Nicolet iS10 spectrometer from 400 to 4000 cm^{-1}. The carbon content of Mn_3O_4/NCDs was determined by TGA analysis (TGA8000). The N_2 adsorption-desorption isotherm was performed on Four-station automatic specific surface and porosity adsorption analyzer (Quadrasorb evo). XPS was acquired by Thermo ESCALAB 250. Raman spectra were obtained on Horiba Jobin Yvon XploRA Raman spectrometer with an excitation wavelength of 785 nm.

Electrochemical measurements

The working electrodes (Mn_3O_4/NCDs and Mn_3O_4) were prepared by pressing the slurries composed of the active material (70 wt.%), Super P (20 wt.%) and polyvinylidene difluoride (10 wt.%). Then, the slurry was uniformly coated onto carbon felt, followed by vacuum drying at 60 °C for 10 h. The average loading of active materials on the electrode slices (diameter: 12 mm) was around 1.5 mg. The zinc foil with a diameter of 16 mm and thickness of 0.2 mm worked as the anode. An aqueous solution containing 2 M of $ZnSO_4$ and 0.2 M of $MnSO_4$ was used as the electrolyte, with glass fiber film (Whatman GF/D glass fiber paper) as the separator. The galvanostatic charge-discharge and rate performance were evaluated by using battery test systems (LAND CT2001A) in the potential range of 0.8–1.8 V versus Zn^{2+}/Zn. CV measurements, GITT and EIS were conducted with a CHI 660E electrochemical workstation. All measurements and assemblies (CR2016-type coin cells) were performed at room temperature.

Acknowledgements

This work was financially supported by the National Natural Science Foundation of China (21975048, 21771039), and the Shanghai Science and Technology Committee (19DZ2270100).

Conflict of Interest

The authors declare no conflict of interest.

Data Availability Statement

The data that support the findings of this study are available from the corresponding author upon reasonable request.

Keywords: carbon dots · cathode material · Mn_3O_4 · nanocomposite · zinc ion battery

[1] a) G. Fang, J. Zhou, A. Pan, S. Liang, *ACS Energy Lett.* **2018**, *3*, 2480–2501; b) H. Jia, Z. Wang, B. Tawiah, Y. Wang, C.-Y. Chan, B. Fei, F. Pan, *Nano Energy* **2020**, *70*, 104523; c) B. Tang, L. Shan, S. Liang, J. Zhou, *Energy Environ. Sci.* **2019**, *12*, 3288–3304.
[2] a) X. Zeng, J. Hao, Z. Wang, J. Mao, Z. Guo, *Energy Storage Mater.* **2019**, *20*, 410–437; b) W. Li, K. Wang, M. Zhou, H. Zhan, S. Cheng, K. Jiang, *ACS Appl. Mater. Interfaces* **2018**, *10*, 22059–22066; c) L. Wang, K.-W. Huang, J. Chen, J. Zheng, *Sci. Adv.* **2019**, *5*, 4279.
[3] a) X. Pu, T. Song, L. Tang, Y. Tao, T. Cao, Q. Xu, H. Liu, Y. Wang, Y. Xia, *J. Power Sources* **2019**, *437*, 226917; b) S. Deng, Z. Yuan, Z. Tie, C. Wang, L. Song, Z. Niu, *Angew. Chem. Int. Ed.* **2020**, *59*, 22002–22006; *Angew. Chem.* **2020**, *132*, 22186–22190; c) N. Wang, X. Dong, B. Wang, Z. Guo, Z. Wang, R. Wang, X. Qiu, Y. Wang, *Angew. Chem. Int. Ed.* **2020**, *59*, 14577–14583; *Angew. Chem.* **2020**, *132*, 14685–14691; d) J. Liu, N. Gong, W. Peng, Y. Li, F. Zhang, X. Fan, *Chem. Eng. J.* **2022**, *428*, 130981.
[4] V. Mathew, B. Sambandam, S. Kim, S. Kim, S. Park, S. Lee, M. H. Alfaruqi, V. Soundharrajan, S. Islam, D. Y. Putro, J.-Y. Hwang, Y.-K. Sun, J. Kim, *ACS Energy Lett.* **2020**, *5*, 2376–2400.

[5] a) X. Gao, H. Wu, W. Li, Y. Tian, Y. Zhang, H. Wu, L. Yang, G. Zou, H. Hou, X. Ji, *Small* **2020**, *16*, 1905842; b) R. Guo, L. Ni, H. Zhang, X. Gao, R. Momen, A. Massoudi, G. Zou, H. Hou, X. Ji, *ACS Appl. Energ. Mater.* **2021**, *4*, 10940–10947.
[6] a) D. Kundu, B. D. Adams, V. Duffort, S. H. Vajargah, L. F. Nazar, *Nat. Energy* **2016**, *1*, 16119; b) J. Long, F. Yang, J. Cuan, J. Wu, Z. Yang, H. Jiang, R. Song, W. Song, J. Mao, Z. Guo, *ACS Appl. Mater. Interfaces* **2020**, *12*, 32526–32535; c) Y. Jiang, D. Ba, Y. Li, J. Liu, *Adv. Sci.* **2020**, *7*, 1902795.
[7] J. Hao, J. Mou, J. Zhang, L. Dong, W. Liu, C. Xu, F. Kang, *Electrochim. Acta* **2018**, *259*, 170–178.
[8] Q. Tan, X. Li, B. Zhang, X. Chen, Y. Tian, H. Wan, L. Zhang, L. Miao, C. Wang, Y. Gan, J. Jiang, Y. Wang, H. Wang, *Adv. Energy Mater.* **2020**, *9*, 2001050.
[9] H. Chen, W. Zhou, D. Zhu, Z. Liu, Z. Feng, J. Li, Y. Chen, *J. Alloys Compd.* **2020**, *813*, 151812.
[10] a) J.-S. Wei, T.-B. Song, P. Zhang, X.-Q. Niu, X.-B. Chen, H.-M. Xiong, *Mater. Chem. Front.* **2020**, *4*, 729–749; b) J.-S. Wei, T.-B. Song, P. Zhang, Z.-Y. Zhu, X.-Y. Dong, X.-Q. Niu, H.-M. Xiong, *ACS Appl. Energ. Mater.* **2020**, *3*, 6907–6914; c) X. T. Zheng, A. Ananthanarayanan, K. Q. Luo, P. Chen, *Small* **2015**, *11*, 1620–1636; d) R. Guo, L. Li, B. Wang, Y. Xiang, G. Zou, Y. Zhu, H. Hou, X. Ji, *Energy Storage Mater.* **2021**, *37*, 8–39.
[11] a) H. Hou, C. E. Banks, M. Jing, Y. Zhang, X. Ji, *Adv. Mater.* **2015**, *27*, 7861–7866; b) C. Hu, M. Li, J. Qiu, Y.-P. Sun, *Chem. Soc. Rev.* **2019**, *48*, 2315–2337; c) B. Yang, R. Jelinek, Z. Kang, *Mater. Chem. Front.* **2020**, *4*, 1287–1288.
[12] J.-S. Wei, H. Ding, P. Zhang, Y.-F. Song, J. Chen, Y.-G. Wang, H.-M. Xiong, *Small* **2016**, *12*, 5927–5934.
[13] X. Niu, T. Song, H. Xiong, *Chin. Chem. Lett.* **2021**, *32*, 1953–1956.
[14] a) Z.-A. Qiao, Y. Wang, Y. Gao, H. Li, T. Dai, Y. Liu, Q. Huo, *Chem. Commun.* **2010**, *46*, 8812–8814; b) K. Jiang, S. Sun, L. Zhang, Y. Lu, A. Wu, C. Cai, H. Lin, *Angew. Chem. Int. Ed.* **2015**, *54*, 5360–5363; *Angew. Chem.* **2015**, *127*, 5450–5453.
[15] a) A.-M. Alam, B.-Y. Park, Z. K. Ghouri, M. Park, H.-Y. Kim, *Green Chem.* **2015**, *17*, 3791–3797; b) X. Wei, X. Jiang, J. Wei, S. Gao, *Chem. Mater.* **2016**, *28*, 445–458.
[16] D. Jarosch, *Miner. Petrol.* **1987**, *37*, 15–23.
[17] a) A. Diallo, N. Tandjigora, S. Ndiaye, T. Jan, I. Ahmad, M. Maaza, *SN Appl. Sci.* **2021**, *3*, 562; b) W. Shen, C. Wang, Q. Xu, H. Liu, Y. Wang, *Adv. Energy Mater.* **2015**, *5*, 1400982.
[18] C. Zhu, G. Fang, J. Zhou, J. Guo, Z. Wang, C. Wang, J. Li, Y. Tang, S. Liang, *J. Mater. Chem. A* **2018**, *6*, 9677–9683.
[19] P. Yu, Y. Zeng, H. Zhang, M. Yu, Y. Tong, X. Lu, *Small* **2019**, *15*, 1804760.
[20] a) W. Sun, F. Wang, S. Hou, C. Yang, X. Fan, Z. Ma, T. Gao, F. Han, R. Hu, M. Zhu, C. Wang, *J. Am. Chem. Soc.* **2017**, *139*, 9775–9778; b) S. Bag, C. R. Raj, *J. Mater. Chem. A* **2016**, *4*, 587–595.
[21] a) C. Huang, Q. Wang, G. Tian, D. Zhang, *Mater. Today Phys.* **2021**, *2*, 100518; b) L. Wang, X. Cao, L. Xu, J. Chen, J. Zheng, *ACS Sustainable Chem. Eng.* **2018**, *6*, 16055–16063.

Manuscript received: November 9, 2021
Revised manuscript received: December 11, 2021
Accepted manuscript online: February 4, 2022
Version of record online: February 19, 2022